Advances in Aircraft and Spacecraft Sciences, *Vol. 7, No. 5 (2020) 441–458*
DOI: https://doi.org/10.12989/aas.2020.7.5.441

Optimal aerodynamic design of hypersonic inlets by using streamline-tracing techniques

Bing Xiong[2a], Michele Ferlauto[*1] and Xiaoqiang Fan[2b]

[1]*Department of Mechanical and Aerospace Engineering, Politecnico di Torino, 10129 Torino Italy*
[2]*College of Aerospace Science and Engineering, National University of Defense Technology, 410073 Changsha, PRC*

(Received January 10, 2020, Revised April 1, 2020, Accepted April 6, 2020)

Abstract. Rectangular-to-Ellipse Shape Transition (REST) inlets are a class of inward turning inlets designed for hypersonic flight. The aerodynamic design of REST inlets involves very complex flows and shock-wave patterns. These inlets are used in highly integrated propulsive systems. Often the design of these inlets may require many geometrical constraints at different cross-section. In present work a design approach for hypersonic inward-turning inlets, adapted for REST inlets, is coupled with a multi-objective optimization procedure. The automated procedure iterates on the parametric representation and on the numerical solution of a base flow from which the REST inlet is generated by using streamline tracing and shape transition algorithms. The typical design problem of optimizing the total pressure recovery and mass flow capture of the inlet is solved by the proposed procedure. The accuracy of the optimal solutions found is discussed and the performances of the designed REST inlets are investigated by means of fully 3-D Euler and 3-D RANS analyses.

Keywords: inward turning inlet; shape transition; aerodynamic optimization

1. Introduction

The inlet plays a relevant role in ramjet/scramjet powered hypersonic vehicles and represents therefore a critical item in the access to the space by Single-Stage-To-Orbit (SSTO) or Two-Stage-To-Orbit (TSTO) systems (Kuranov and Korabelnikov 2008, Cui *et al.* 2013). The inlet must decelerate and compress the flow with minimal skin-friction, shock and heat transfer losses, while dealing with complex shock patterns and providing an optimal mass-flow capture-area and a uniform flow at the combustor inlet.

Different types of hypersonic inlets have been evaluated in the past. Two-dimensional ramp-like inlets were favored because of the simpler design. Axisymmetric Busemann and

*Corresponding author, Associate Professor, E-mail: michele.ferlauto@polito.it
[a]Ph.D., E-mail: xiongbing10@nudt.edu.cn
[b]Professor, E-mail: xiaoqiangfan@hotmail.com

http://www.techno-press.org/?journal=aas&subpage=7 ISSN: 2287-528X(Print), 2287-5271(Online)

streamtraced Busemann inlets stand out of many two-dimensional inlets because of their high compression efficiency and good mass capture performances (Kothari *et al.* 1996, You 2011). This kind of inlets are therefore good candidates for hypersonic air-breathing aircrafts (Mölder and Szpiro 1966, Kothari *et al.* 1996, Billig *et al.* 1999). Theoretically, these inlets have significantly higher efficiencies than conventional two-dimensional designs. Considering the practical application, the entrance shape of a hypersonic inlet is restricted by the integration requirement, whereas the exit shape is restricted by the downstream combustor. However, the entrance shape and the exit shape cannot be controlled at the same time by applying streamline tracing technique. Moreover, the actual performance of these inlets may be affected by many details as finite leading edge truncation angles and bluntness and boundary layer displacement (Drayna *et al.* 2006).

To solve the design problem, a method of shape transition was introduced and inward turning inlets with a Rectangular-to-Ellipse Shape Transition (REST) were designed and tested experimentally at flight Mach number $M_o = 6$ (Smart 1999, 2001). The design technique has been improved enabling the integration with arbitrary body shapes (Gollan and Smart 2013).

Since the interest in inward-turning inlets has been renewed, more accurate and performing numerical tools have been implemented (Xiong *et al.* 2019a), making easier the integration with vehicle airframe (Liu *et al.* 2014, Ding *et al.* 2019), as well as with ramjet/scramjet combustors of circular or elliptical inlet sections (Degregori and Ferlauto 2018, Xiong *et al.* 2019b). Intake on-design and off-design conditions have been studied (Ramasubramanian *et al.* 2008). Moreover, optimization methodologies have been introduced in the design process to improve the performance (Wang *et al.* 2017).

In present work, a multi-objective optimization of the REST inlet, based on the NSGA-II genetic algorithm, is investigated. The propose numerical procedure introduces a parameterization of the truncated Busemann inlet, namely the "base flow", having desired compression and area contraction features. The inward-turning REST inlet is then obtained by a combination of the streamline-tracing and shape-transition approaches. The design procedure is driven by the multi-objective optimization NSGA-II genetic algorithm. Faster, inviscid evaluations of the flowfield and of the objective functionals are used in the inner loop of optimization. The accuracy of the design solution is then checked and improved by fully 3-D Euler or RANS flowfield analyses. Effectiveness of the method and comparisons of the different level of flow modelization at on-design and off-design conditions has been performed. The plan of the paper is as follows: first the base flow parametrization and the streamline-tracing and shape-transition algorithms are described; then the multi-objective optimization technique is illustrated. Finally, the results of the design procedure are analyzed and compared.

2. MATHEMATICAL MODEL

2.1 Parameterization of the base flow

The inward-turning inlet is generated as a stream-tube extracted from a reference flowfield defined here as the *base flow*. This base flow is assumed axisymmetric and governed by the

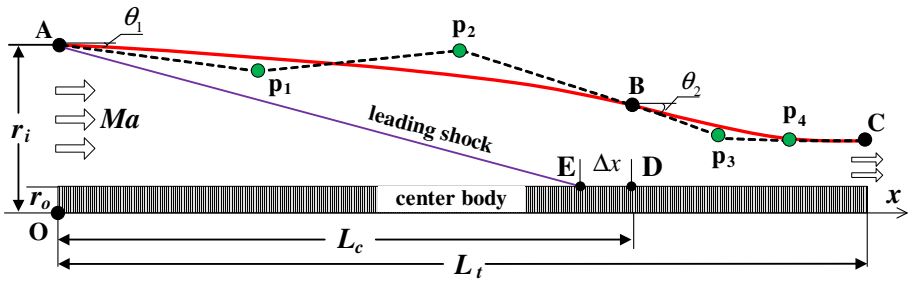

Fig. 1 Design parameters of the reference flowfield onto the meridional plane. Shock reflections/generation near points E and D has been omitted for clarity.

compressible Euler equations. The main objective of the basic flow is the deceleration of the supersonic stream according with some prescribed flow features. The underlying idea is that any extracted stream-tube, i.e. the intake, will maintain the main features of the flow in which is embedded, that is, of the base flow.

As shown in Figure 1, we assume the base flow as generated by a converging axisymmetric duct, confined within an inner wall surface of constant radius r_o, and an outer wall of general shape. The flow entering this duct at hypersonic speed give rise to a conical shock at the inlet section. This shock is then reflected by the inner wall. If the reflection point is assumed as the cowl lip, an optimal intake configuration with a shock on lip can be identified according to classical approaches, e.g. Busemann (1942). In present approach we consider a more general configuration, depicted in Figure 1, where the leading shock, departing from point A, may be reflected at a point E different from the cowl lip (point D). The mismatch between the two points is defined as $\Delta x = x_{\mathrm{D}} - x_{\mathrm{E}}$ and will be minimized by the optimization procedure. It must be stressed also that the shock structure at the cowl lip is influenced by slope of the outer wall near point B, that is, from the angle θ_2. The cylindrical center-body of radius r_o has been introduced in order to avoid the generation of a Mach disk that may lead to large total pressure losses (Hornung 2000). The outer wall geometry is composed by two Quasi-Uniform B-Splines (QUBS) curves. The QUBS control points are shown in Figure 2 as points A, P_1, P_2, B, P_3, P_4, C. The outer wall AC is divided into two segments at point B, ($x_{\mathrm{B}} = x_{\mathrm{D}}$) and each curve is generated using a third-order QUBS which has four control points. The total length of base flow is L_t. The cowl lip is located at point D ($x_D = L_c$). All lengths are normalized by the entrance radius R_i that has been also set as the reference length throughout the paper.

The key parameters of the base flow, which are controlled by varying the QUBS control points, are:
(i) the global area contraction ratio, defined as the ratio between the inlet and exit area

$$\mathrm{CRT}_b = \frac{r_{\mathrm{A}}^2 - r_o^2}{r_{\mathrm{C}}^2 - r_o^2} \tag{1}$$

(ii) the internal area contraction ratio, that is, the ratio of the area at the cowl lip section

and at exit section

$$\mathrm{CRI}_b = \frac{r_{\mathrm{B}}^2 - r_o^2}{r_{\mathrm{C}}^2 - r_o^2} \tag{2}$$

(iii) the inlet ramp angle of the outer wall

$$\tan\theta_1 = \frac{r_{\mathrm{A}} - r_{\mathrm{P}_1}}{x_{\mathrm{A}} - x_{\mathrm{P}_1}} \tag{3}$$

(iv) the slope of the outer wall near the cowl inlet section (i.e. the slope at point B)

$$\tan\theta_2 = \frac{r_{\mathrm{B}} - r_{\mathrm{P}_2}}{x_{\mathrm{B}} - x_{\mathrm{P}_2}} = \frac{r_{\mathrm{B}} - r_{\mathrm{P}_3}}{x_{\mathrm{B}} - x_{\mathrm{P}_3}} \tag{4}$$

The values of the angles θ_1, θ_2 are obtained according to the Eq. 3 and Eq. 4, respectively. The parameters defined in Eqs. 1–4 allow the designers to express the main features of the compression wall on the basis of meaningful parameters instead of less intuitive variations of the QUBS control points.

2.2 Flow governing equations and numerical method

In this section the flow models used throughout the work and the related computational method are outlined. The proposed design procedure is based mainly on three different flow models: (i) the axisymmetric compressible Euler equations are used for solving the base flow; (ii) the fully 3-D compressible Euler equations and (iii) the 3-D compressible Reynolds Averaged Navier-Stokes (RANS) equations are adopted for the simulation of the flow inside and around the REST inlet. Several solvers have been used, including commercial software (e.g. Ansys Fluent 19.2), open source (OpenFoam) and in-house codes (Ferlauto and Marsilio 2014, 2016, 2018), according to the hardware platform and computational task of the optimization procedure. All solvers used are able to deal with compressibility effects and supersonic flows. The governing equations are written in conservative form including the conservation equations for mass, momentum, and energy, along with the equation of ideal gas. The dynamic viscosity is solved by Sutherland's law. A second-order upwind scheme is used in the spatial discretization, with slope-limited nonlinear reconstruction of the solution and adaptive time stepping. Either explicit or implicit density-based algorithms are used to solve the equations with shock capturing schemes based on several flux difference splitting methods (e.g. Roe FDS). Boundary conditions are imposed according to the characteristics based approach of Poinsot and Lele (1992) The above mentioned computational methods have been applied successfully for solving similar viscous hypersonic flows in (Wang *et al.* 2015). As in that case, we adopt the *k-ω SST* model for turbulence modeling.

2.3 Streamline tracing and shape transition algorithm

In this section we describe the procedure for generating the final inward-turning inlet from a sequence of streamtubes extracted from the base flow. Once the numerical solution of a steady flowfield is computed (e.g. see Figure 2), streamlines passing for a generic point of the domain can be computed easily from the velocity field. This task can be performed by many software for CFD visualization (e-g- Paraview, Visit, Tecplot).

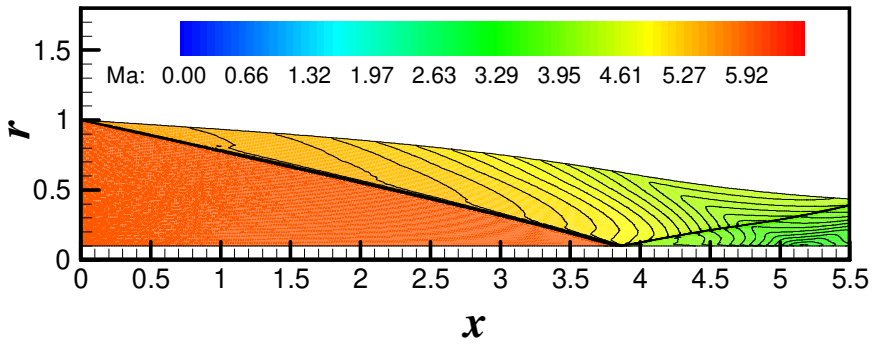

Fig. 2 Mach contours on the axisymmetric base flowfield (truncated).

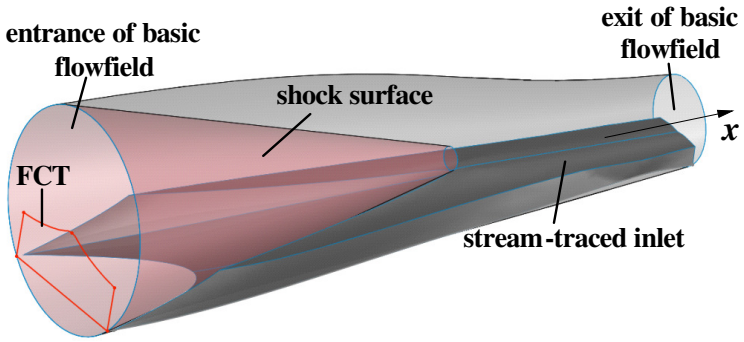

Fig. 3 Sketch of the stream-traced inlet.

The boundary surface of a streamtube can be deduced by setting a cloud of point on the boundary of a generic section and by extracting the corresponding streamlines in the base flow. By interpolation, this surface can be defined by a mesh $\mathcal{G}(x, y, z) = f(u(x, r), v(x, r))$, being (u, v) the velocity components of the axisymmetric base flow. Finally, the shape of the inlet surface is obtained as the difference between the stream-tube and the conic surface on the inlet shock (shock-on-lip case) or the conic surface obtained by revolving the segment A-D about the x-axis. The former case is represented in Figure 3.

The streamline tracing technique does not allow for the control of the intake shape in more than one section. By following the approach proposed by Smart (1999) for imposing many geometric constrains or features at different sections, a streamtube satisfying each condition is computed by streamline tracing and a shape transition method is applied in order to combine all streamtubes (Smart (1999), Barger (1981).

Figures 4-5 present this process of stream tracing and shape transition. Without loss of generality, we considered the REST inlet obtained by combining two stream-traced inlets only: one has a rectangular-like entrance (Shape-A) and the other one has an elliptical exit section (Shape-B). If additional shape constraints are required at other sections, the shape transition algorithm must be applied to the corresponding streamtubes between two

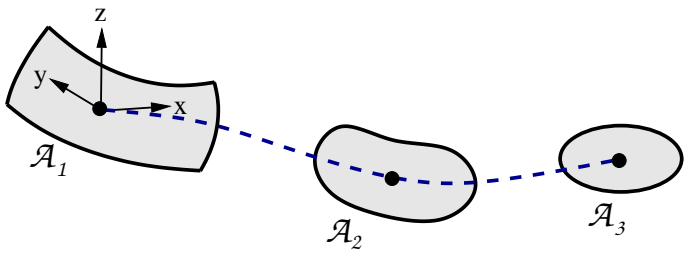

Fig. 4 Rectangular-to-elliptic shape transition.

subsequent sections.

A rectangular-like projection of the inlet shape at $x = x_{\mathrm{A}}$ is defined first, and the stream-traced inlet surface $\mathcal{G}_{\mathrm{A}}$, i.e. Shape-A, is computed. At the base flow exit section $x = x_{\mathrm{C}}$, an elliptic section is computed, on a mass averaged basis of the curve $\mathcal{G}_{\mathrm{A}}(x_{\mathrm{C}})$, able to swallow the the massflow of inlet Shape-A. A new inlet surface $\mathcal{G}_{\mathrm{B}}$ is derived after streamline tracing the elliptic section backwards in the base flow, thus obtaining Shape-B. The combination of inlets is based on the procedure proposed by Barger (1981). Given the functional representations $\mathcal{G}_{\mathrm{A}}(x, r, \varphi)$ and $\mathcal{G}_{\mathrm{B}}(x, r, \varphi)$ of the stream-traced inlet surfaces, then the lofted values in their blending are computed as:

$$\mathcal{G}_{\mathrm{I}}(x, r, \varphi) = \mathcal{G}_{\mathrm{A}}(x, r, \varphi)^{E(x)} \mathcal{G}_{\mathrm{B}}(x, r, \varphi)^{1-E(x)} \tag{5}$$

where

$$E(x) = \left(\frac{x_{\mathrm{B}} - x}{x_{\mathrm{B}} - x_{\mathrm{A}}} \right)^{\alpha} \tag{6}$$

and $\alpha > 0$ is an arbitrary parameter that provides a means of adjusting the rate at which the shape changes. It may be assigned as a constant or as a smooth function of x. The lofted inlet surface is based on an inviscid flowfield. In practice, boundary layer growth will reduce the available area for the core flow. This reduction of area would lead to an effective compression ratio larger than intended. To correct for this, the surface should be enlarged by considering the development of the boundary layer within the inlet. It is difficult to perform a rigorous boundary layer calculation for this complex 3D geometry. For design purposes, the small crossflow assumption could be used when calculating boundary layer displacement thickness.

3. Optimization.

The inlet performances are related to the mass-flow capture area and to the aerodynamic losses. In general, the former variable is controlled by imposing the area of the inlet entrance and the area contraction ratios. The fluid losses depend on the shock structure and on the internal compression and skin-friction. Optimal performances are therefore reached by tending towards the shock-on-lip configuration $\Delta x \to 0$ and by maximizing the total pressure recovery $\sigma_p = P_c^o / P_a^o$. We are then lead to a multi-objective optimization aiming to minimize the following functionals

$$\mathcal{J}_1 = |\Delta x|, \qquad \mathcal{J}_2 = -\sigma_p \tag{7}$$

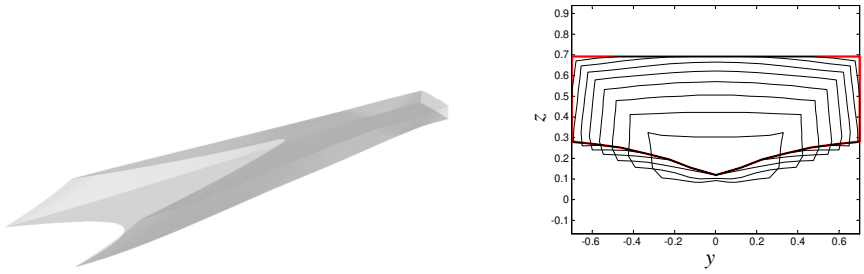

(a) Rectangular Inlet (Shape-A)

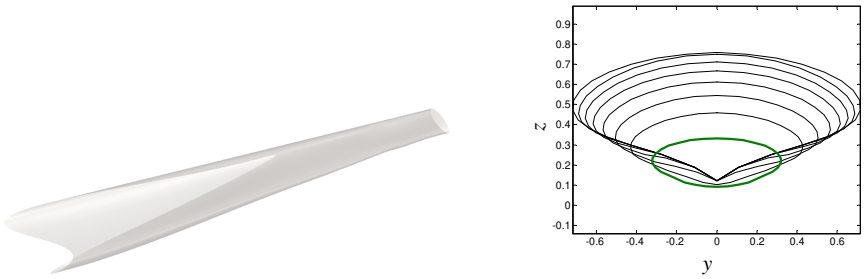

(b) Elliptic Outlet (Shape-B)

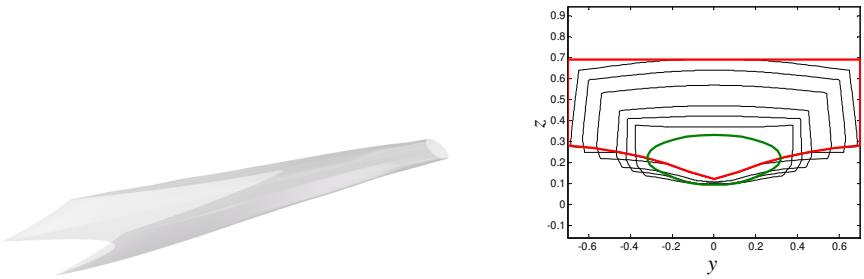

(c) Rectangular-to-Elliptic-Shape-Transition

Fig. 5 Generation of a REST inlet by shape transition.

The control variable of present optimization are deduced from the parameterization of the base flow discussed in previous sections. Briefly, we have two different sets of parameters to deal with. One set is describing the base flow boundary, another one defines the stream-tracing process. We selected the former set, that is supposed of much greater impact on the intake design. In fact, stream-traced inlet will mostly maintain the same features of the corresponding base flow. The base flow boundary is defined by means of two third-order QUBS, with four control points each. By enforcing the boundary continuity, the set of controls is formed by the 14 variable, i.e. the coordinates (x_j, r_j) of points A, B, C, P_1, P_2, P_3 and P_4 . Moreover, Eqs.1-4 must be satisfied. Aiming to reduce the computational cost and to enhance the convergence rate of the optimization, additional constraints to the control points have been introduced. The axial positions x_{p_1}, x_{p_2}, x_{p_3}, and $r_{p_4} = r_{\mathrm{C}}$ of

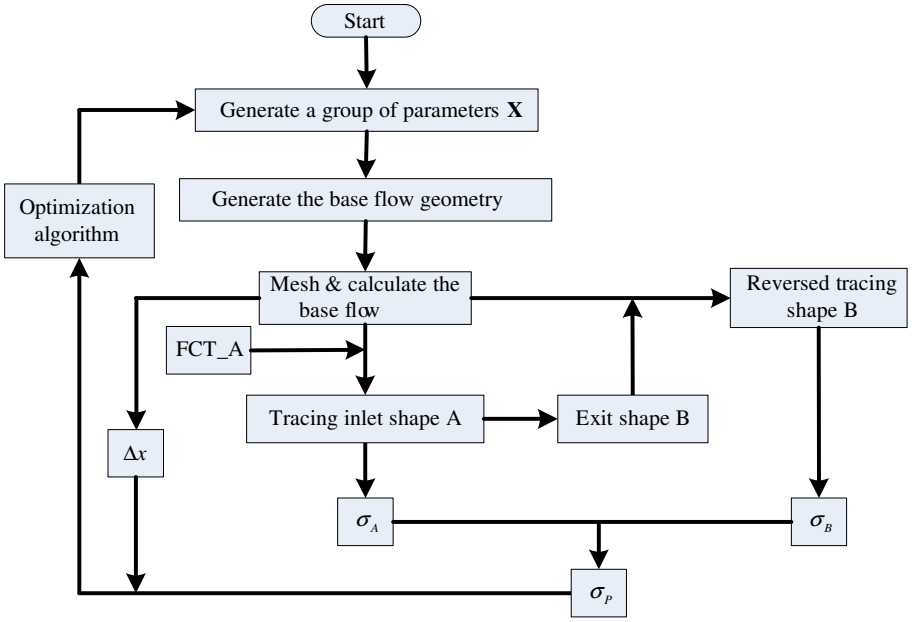

Fig. 6 Scheme of the optimization procedure and its integration with the streamline tracing and shape transition algorithms.

the QUBS control points are assigned. The latter condition enforces a zero slope at the base flow outlet boundary. In so doing, there are only three free parameters left, namely $\boldsymbol{Y} = [r_{p_1}, r_{p_2}, x_{p_4}]$. Actually, we prefer a more meaningful set of controls $\boldsymbol{X} = [\theta_1, \theta_2, x_{p_4}]$ which is anyway equivalent to the set Y.

After bounding the range of controls to values suitable for a practical design, we are lead to the optimization problem expressed as follows

$$\min(\, \mathcal{J}_1(\boldsymbol{X}),\, \mathcal{J}_2(\boldsymbol{X})\,) \tag{8}$$

subjected to

$$\begin{cases} 0 \le \theta_1 \le 13^o \\ 0 \le \theta_2 \le 20^o \\ (2x_{\mathrm{B}} + x_{\mathrm{C}})/3 < x_{p_4} < x_{\mathrm{C}} \end{cases} \tag{9}$$

The constrained optimum problem (7–9) is solved numerically by using the Non-dominated Sorting Genetic Algorithm II (NSGA-II) of optimization (Deb *et al.* 2002). NSGA-II generates off-springs using a specific type of crossover and mutation and then it selects the next generation according to non-dominated sorting and crowding distance comparison.

A sketch of the optimization procedure is sketched in Figure 6. Briefly, starting from a initial set of parameters $\boldsymbol{X}_o$, the control points of the QUBS defining the outer boundary are deduced. A mesh is generated and the axisymmetric base flowfield is computed numerically. At this stage the flow is assumed as inviscid.

The stream-traced inlets Shape-A and Shape-B are computed and shape transition is applied in order to generate the REST inlet. The objective functionals of Eq. 7 and the

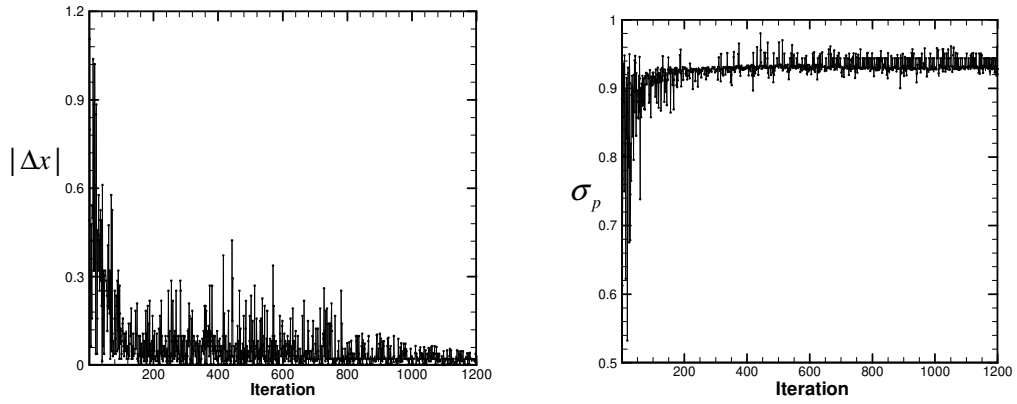

(a) (b)

Fig. 7 Convergence history of the objective functionals (a) $|\Delta x| = \mathcal{J}_1$ and (b) $\sigma_p = -\mathcal{J}_2$ during the optimization process.

functional residuals are computed. If the convergence criteria are not matched, the optimization algorithm is applied and a new set of parameters $\boldsymbol{X}_k$ is derived for the new iteration step k.

The optimization procedure has been carried out inside the ISIGHT framework, an efficient tool for combining together different software and codes, thus achieving automation of parameterization, simulation, and optimization.

The optimization procedure may have different levels of accuracy and computational costs, according to different accuracy in computing the REST inlet performances. The procedure depicted in Figure 6 refers to the fastest approach, which deduces an estimation of the REST inlet performances from those of the two inlets Shape-A and Shape-B. For instance, a fast estimation of the objective functional $\mathcal{J}_2$ is

$$\mathcal{J}_2 = -\sigma_p = -(\sigma_{\mathrm{A}} + \sigma_{\mathrm{B}})/2 \tag{10}$$

More accurate analyses require the computation of the fully three-dimensional flow on the REST inlet, either in the inviscid or viscous case. In next sections the different approaches are compared in terms of costs and accuracy.

4. Numerical results

4.1 REST inlet optimization

In this section numerical results about a REST inlet optimization are presented and the main findings are discussed. The relevant design parameters we selected are as follows

$$M_o = 6, \quad r_o = 0.1 \quad r_{\mathrm{A}} = 1, \quad x_{\mathrm{A}} = 0, \quad x_{\mathrm{B}} = 3.9, \quad x_{\mathrm{C}} = 5.5, \quad \mathrm{CRT}_b = 6.6, \quad \mathrm{CRI}_b = 2.5$$

and they are kept constant during the optimization experiments. The cowl lip abscissa is set to $x_{\mathrm{D}} = L_c = x_{\mathrm{B}}$. The constraints (9) are enforced to reduce the number and range of

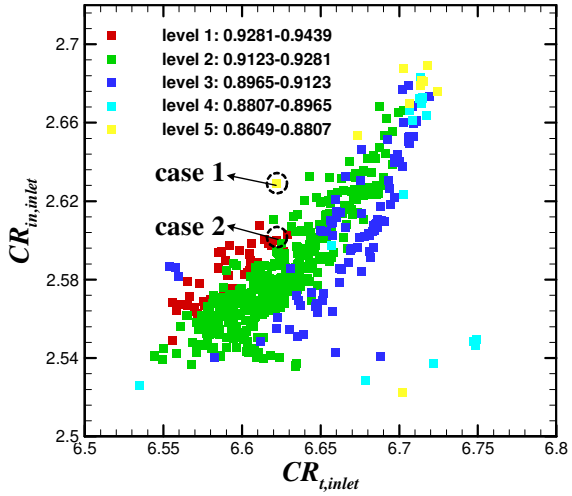

Fig. 8 Total and internal area contraction ratios of the REST inlet configurations obtained during the optimization process. Only the solutions having $\Delta x/L_c < 0.01$ are displayed.

control variables. As described in Section 3, an initial set of parameters $\boldsymbol{X}_o$ is guessed and the control points of the QUBS defining the outer boundary of the base flow are deduced. A typical solution of the axisymmetric base flow computed numerically during the optimization, is presented in Figure 2.

Concerning the setup of the optimizer, which is based on the NSGA-II algorithm, the population size and the number of generations are set to 24 and 60, respectively. The crossover probability is 0.5 .

The optimization histories of the two objectives $\mathcal{J}_1$ and $\mathcal{J}_2$ throughout the procedure are shown in Figure 7. As visible in the diagrams, optimal solutions very close to the shock-on-lip configuration and having high total pressure recovery σ_p are obtained in about one hundred iterations. On average, during these iterations the value of Δx is reduced of one order of magnitude and σ_p is increased of about the 25% . An initial assumption we may now check is if the REST inlet configurations obtained are preserving the main features of the original base flow. By computing the intake cross-sections areas at the entrance (A_i), at the cowl lip (A_c) and at the exit (A_e), the area contraction ratios $\text{CRT}_i = A_i/A_e$ and $\text{CRI}_i = A_c/A_e$ for the REST inlet can be defined. Inlet contraction ratios can be then computed and compared with the design values of the base flow. From a sensitivity analysis carried out during the optimization, we observed that the mass flow capture of the shock-on-lip case is almost reached when $\Delta x/L_c < 1\%$. We therefore assumed as "$\mathcal{J}_1$-optimal" any REST inlet solution that satisfies this condition, because it implies that the inviscid inlet will have almost full mass capture under design conditions.

Obviously, all these optimal inlets will not have the same predicted total pressure recovery coefficients σ_p. Figure 8 shows all $\mathcal{J}_1$-optimal inlets obtained during the optimization. Each solution is represented by a $(\text{CRT}_i, \text{CRI}_i)$ pair in the plot. The solutions are divided into 5 levels according to the corresponding value of σ_p. The range for each level is shown in the

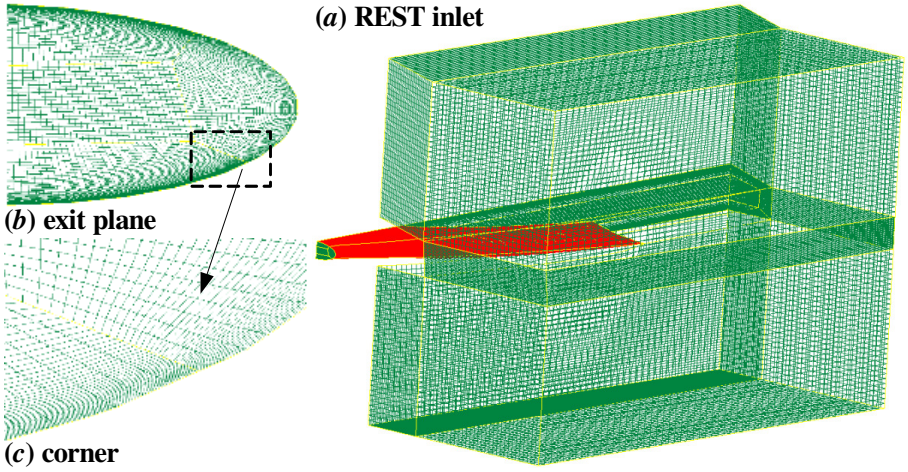

Fig. 9 Sketch of the multi-block three-dimensional mesh inside and around the REST inlet.

figure. As illustrated, inlets of level 1 have the highest σ_p, inlets of level 5 have the lowest. According to the convergence process, level 5 points are most located in the early stage of optimization, whereas level 1 points are most obtained in the late stage of the process. All these solutions are spread in a range of area contraction ratios higher than the nominal values $(\mathrm{CRT}_b, \mathrm{CRI}_b)$ of the base flow, e.g. $6.55 < \mathrm{CRT}_i < 6.75$ and $2.54 < \mathrm{CRI}_i < 2.68$.

This shift can be alleviated eventually by an area correction algorithm accounting for boundary layer effects. Since a CFD analysis of the 3-D flow is planned, at least the end of the optimization procedure, this step is neglected.

Let us note instead that all solutions along a vertical line in Figure 8 have the same CRT_i, the same lengths L_t and cowl lip position L_c, the same cowl inlet and exit areas and they generate almost the same shock-on-lip configuration at the same design flight Mach number M_o. We carried out a deeper analysis of two configuration, presented as Case-1 and Case-2 in the plot, in order to identify the key parameters leading to higher total pressure recovery factors σ . According to the plot, the solutions Case-1 and Case-2 are rated level 5 and level 1, respectively. The main geometrical parameters of the two configurations are resumed in Table 1 . Since the σ_p-values in Figure 8 are estimated from the stream-traced solutions on the base flow, they may be inaccurate. For this reason, full three-dimensional CFD computations of the flow around and inside the two inlet configurations have been carried out for comparison.

Table 1 Design parameters of Case-1 and Case-2 inlets.

	L_c (m)	L_c/L_t	CRT_i	CRI_i	$\Delta x/L_c$ (%)
Case-1	1.365	0.71	6.62	2.63	0.8
Case-2	1.365	0.71	6.62	2.60	0.6

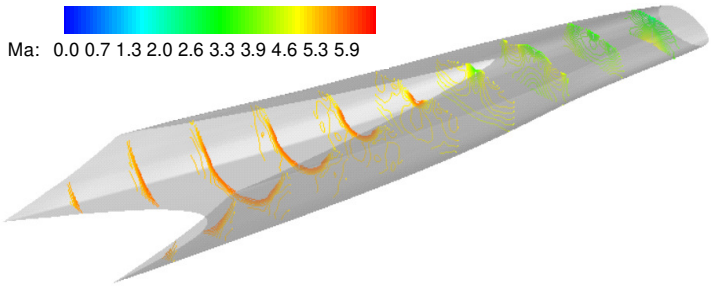

(a) Case-1

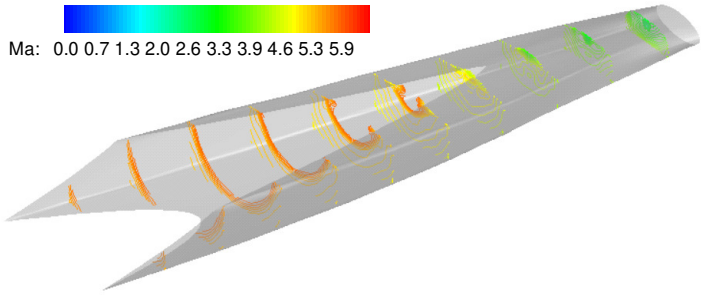

(b) Case-2

Fig. 10 Intake geometry and Mach contours of the inviscid CFD solution for (a) Case-1 and (b) Case-2 REST inlets.

4.2 On-design and off-design aerodynamic analysis

In this section the analysis of the CFD simulations of the flow inside the selected REST inlet configurations (Case-1 and Case-2) are illustrated. Both on-design and off-design conditions are considered. The computations have been performed for both the 3-D inviscid and viscous case and compared. A multi-block grid around and inside the REST inlet has been generated, as shown in Figure 9. Only half intake is considered, because the computational domain is symmetric and no cross-wind is considered.

The fully 3-D computations of the flowfield by using the compressible Euler equations are shown in Figure 10 . The inlet geometry and iso-Mach lines at different sections are shown for Case-1 and Case-2. The shock surface fits with the 3-D leading edge in both intake configurations. In the inviscid case, the shock-on-lip condition is obtained and both inlets have almost the design mass-flow. The massflow capture ratio ψ for the inlet is defined as

$$\psi = \dot{m}_e/\dot{m}_{capture} = \dot{m}_e/(\rho u)_\infty A_{fct}$$

where $\dot{m}_e$ is the mass-flow rate at the intake exit. The capture area A_{fct} is defined from the intake entrance cross-section, as sketched in Figure 3 . The mass capture ratios for both inviscid computations are almost at 100%, as shown in Table 2. We may argue therefore that the stream-tracing with shape transition design technique is able to match the main features of the 3D inviscid flow inside the inlet.

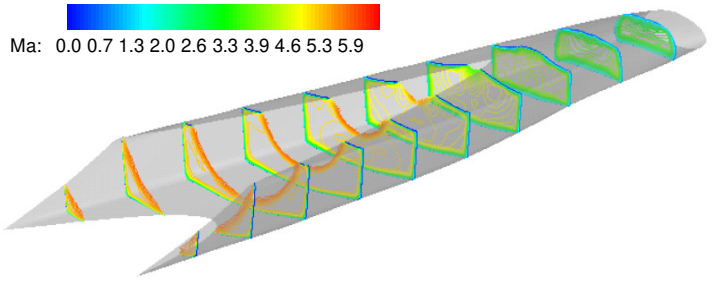

(a) Case-1

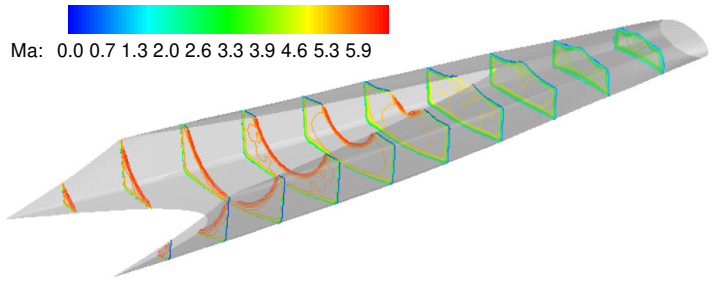

(b) Case-2

Fig. 11 Intake geometry and Mach contours of the viscous CFD solution for (a) Case-1 and (b) Case-2 REST inlets.

The CFD computations of the viscous flow are based on the compressible RANS equations coupled to the $k-\omega$ SST turbulence model. A grid dependency study has been performed. As a result, multi-block structured grid with about 1.5 million nodes has been selected for the discretization of the half-inlet interior and exterior domains. Adiabatic no-slip boundary conditions have been imposed at inlet walls. Wall functions were used to resolve the turbulent boundary layer up to $y^+ \simeq 10$.

The computed flowfields at design conditions for Case-1 and Case-2 are shown in Figure 11 . The leading shock surface does not fit perfectly with the 3-D leading edge of the intake, and a mass flow spillage occurs. This fact is motivated by the boundary layer blockage effect inside the inlet and also by shock-boundary layer interactions. As a result, the mass-flow capture ratios for Case-1 and Case-2 decrease up to 98.3% and 97.5%, respectively. It is anyway visible from the flowfield at different cross-sections depicted in Figure 11 that the boundary layer remains attached around internal walls of the inlets. The inlets performances, computed in the inviscid and viscous case, are resumed in Table 2. The total pressure recovery coefficients σ are also presented in this table. Not surprisingly, the estimated pressure recovery factor σ_p, that obtained by 3-D Euler σ_{inv} and that computed by RANS simulations σ_{vis} are lower and lower. Nevertheless, as long as the approximation σ_p reflects the same relationship of the actual σ_{vis} with respect to the control variables $\boldsymbol{X}$, the use of the former as objective functional of the optimization is fully motivated. Moreover, let us note from Table 2 that the pressure recovery improvements between the two

Table 2 Performances of Case-1 and Case-2 REST inlets at the design point.

	σ_{inv}	ψ_{inv}	σ_{vis}	ψ_{vis}
Case-1	0.888	99.3%	0.688	98.3%
Case-2	0.926	99.8%	0.735	97.5%
improvement	4.3%	–	6.8%	-0.8%

configurations are of the same order, either if measured by using σ_{inv} (4.3%) or σ_{vis} (6.8%) .

The accuracy on performance evaluation of the final design solutions can be then improved in a subsequent step by deeper CFD analyses. The performance mismatch observed can be eliminated by a fully viscous 3D optimization based on RANS simulations. This requires anyway a 3-D parameterization of the complete inlet in order to update its geometry during optimization in an efficient way.

Finally, the CFD analysis has been extended to off-design conditions in order to test the effectiveness of the design solutions to different operating conditions. The flight Mach number M_o has been reduced from 6 up to 4.5 and RANS simulations of the flow have been carried out for both Case-1 and Case-2. The effect of different inflow Mach numbers on the inlet total pressure recovery is illustrated in Figure 12. The trend of the curves on the plot can be explained by considering the changes in the shock-wave pattern when M_o is varied. At the design Mach number, the inlet exhibits a shock-on-lip pattern. When the inflow Mach number is decreased, the leading-edge shock-wave angle β increases, according to the Taylor-Maccol relations (Anderson 1982) also depending on the angle θ_1. The shock-on-lip configuration is lost. Moreover a secondary shock wave is generated at cowl lip, where the flow is subjected to a deflection of an angle close to θ_2. We may therefore argue that the total pressure recovery will increase for decreasing inflow Mach numbers, because of the weaker strength of the shock-waves involved, and also depending on the values of angles θ_1 and θ_2. The actual scenario is then complicated by fully three-dimensional effects, boundary layers and turbulence.

4.3 Design framework performances

We report finally some considerations about the effectiveness and performances of the proposed design procedure. Let us note that the aerodynamic design of devices in supersonic/hypersonic flows is very challenging. Often, one has to dealt with complex shock structures, whose high non-linear behaviour leads to very different flow patterns even with small changes of the device geometry (Drayna *et al.* 2006). Design methods based on the solution of a direct problem, e.g. classical shape optimization approaches, assign and modify parametrically the device geometry but have less control on the generated flowfield. Conversely, approaches based on the solution of inverse problems may impose the desired flow features, but have a weaker control on the geometry (Ferlauto 2015). As a cure for both methods, penalization can be introduce in the optimization problem, thus leading to slower convergence rates.

In our design problem both the flowfield and the intake geometry are subjected to con-

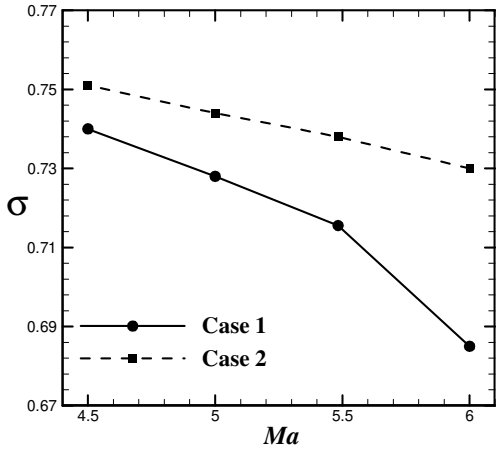

Fig. 12 Computed total pressure recovery factors σ for the REST inlets in off-design conditions.

straints. The approach proposed here generates a solution that matches all the prescribed requirements at each iteration. Then the solution is driven by a multi-objective optimizer. The overall method can be implemented easily in an parallel environment, so that the computational time may vary from a day on a Intel Xeon-based workstation to some hours in an HPC system.

From a flow modelling perspective, approaches based on the Method of Characteristics (MOC) are faster, but very difficult to manage in a fully three-dimensional flowfield. Moreover fitting techniques for shock treatment are required (Degregori and Ferlauto 2018). The adopted approach based on the compressible Euler equations with shock-capturing features is then a good compromise (Ramasubramanian *et al.* 2008). With respect to the full RANS simulations still retains much of the flow features without the one-order increase of the computational time for each design iteration. Moreover, viscous correction can be applied at the end of the process by a limited number of RANS calculations.

Concerning the optimization process, better convergence rates could be obtained by using adjoint optimization approaches but at the cost of an higher complexity of the optimization method (Iollo *et al.* 2001, Ferlauto 2013). As long as the number of design variables remains small, the advantages of these approaches remain limited.

5. Conclusions

A numerical procedure for the optimal design of rectangular-to-elliptic shape transition inlets has been proposed. The procedure is able to deal with more generic shapes and can enforce geometrical constraints to more than two sections of the inlet.

The procedure introduces a parameterization of an axisymmetric base flow, we may also describe as the flow inside a truncated Busemann inlet having desired compression and area contraction features. Once the base flow is solved numerically, the REST inlet is obtained by a combination of the streamline-tracing and shape-transition algorithms. A multi-objective optimization of the REST inlet based on the NSGA-II genetic algorithm is implemented.

Faster evaluations of the flowfield and objective functional estimation are used in the inner loop of optimization. The accuracy of the design solution has been tested and compared with fully 3-D RANS flowfield analyses. Effectiveness of the method has been shown and comparisons between the different levels of flowfield modeling inside the hypersonic intake at on-design and off-design conditions have been performed. The optimization procedure has shown good performances at a reasonable computational cost.

Acknowledgments

The authors gratefully acknowledge the support of the NSFC (No. 11572347 and 11872071) and the China Scholarship Council (CSC). Computational resources were provided by hpc@polito.it, a project of Academic Computing within the Department of Control and Computer Engineering at the Politecnico di Torino.

References

Anderson, J. (1982), *Modern Compressible Flow with Historical Perspective*, McGraw-Hill,New York, USA.

Barger, R.L. (1981), "A procedure for designing forebodies with constraints on cross-section shape and axial area distribution", *Scientific and Technical Information Branch, Hampton, USA*.

Billig, F., Baurle, R. and Tam, C. (1999), "Design and analysis of streamline traced hypersonic inlets",*9th Int. Space Planes and Hypersonic Syst. & Technol. Conf., Norfolk, VA*. https://doi.org/10.2514/6.1999-4974

Busemann, A. (1942), "Die Achsenssymmetrische Kegelizeuber-Schallstromung", *Luftfahrtforschung*, **19**, 137–144.

Cui, K., Hu, S., Li, G., Qu, Z. and Situ, M. (2013), "Conceptual design and aerodynamic evaluation of hypersonic airplane with double flanking air inlets", *Sci. China Technol. Sc.*, **56**, 1980–1988. https://doi.org/10.1007/s11431-013-5288-0

Deb, K., Pratap, A., Agarwal, S. and Meyarivan, T. (2002), "A fast and elitist multiobjective genetic algorithm: NSGA-II", *IEEE Trans. Evol. Comp.*, **6**(2), 182–197. https://doi.org/10.1109/4235.996017

Degregori, E. and Ferlauto, M. (2018), "Optimal aerodynamic design of scramjet facility nozzles", *AIP Conf. Proc.*, **1978**(1), 470114. https://doi.org/10.1063/1.5048596

Ding, F., Liu, J., Huang, W., Peng, C. and Chen, S. (2019), "An airframe/inlet integrated full-waverider vehicle design using as upgraded aerodynamic method", *Aeronaut. J.*, **123**(1266), 1135–1169. https://doi.org/10.1017/aer.2019.49

Drayna, T.W., Nompelis, I. and Candler, G. (2006), "Hypersonic inward turning inlets: design and optimization", *AIAA Paper 2006-297, 44th AIAA Aerosp. Sci. Meeting & Exhibit, Reno, NV*. https://doi.org/10.2514/6.2006-297

Ferlauto, M. (2013), "Inverse design of internally cooled turbine blades based on the heat adjoint equation.", *Inverse Probl. Sci. En.*, **21**(2), 269–282. https://doi.org/10.1080/17415977.2012.693079

Ferlauto, M. (2015), "A pseudo-compressibility method for solving inverse problems based on the 3D incompressible Euler equations.", *Inverse Probl. Sci. En.*, **23**(5), 798–817. https://doi.org/10.1080/17415977.2014.939653

Ferlauto, M. and Marsilio, R. (2014), "A computational approach to the simulation of controlled flows by synthetic jets actuators.", *Adv. Aircraft Spacecraft Sci*, **2**(1), 77–94. https://doi.org/10.12989/aas.2015.2.1.077

Ferlauto, M. and Marsilio, R. (2016), "A numerical method for the study of fluidic thrust vectoring", *Adv. Aircraft Spacecraft Sci*, **3**(4), 367–378. https://doi.org/10.12989/aas.2016.3.4.367

Ferlauto, M. and Marsilio, R. (2018), "Numerical simulation of the unsteady flowfield in complete propulsion systems", *Adv. Aircraft Spacecraft Sci*, **5**(3), 349–362. https://dx.doi.org/10.12989/aas.2018.5.3.349

Gollan, R. and Smart, M. (2013), "Design of modular shape-transition inlets for a conical hypersonic vehicle", *J. Propul. Pow.*, **29**(4), 832–838. https://doi.org/10.2514/1.B34672

Hornung, H. (2000), "Oblique shock reflection from an axis of symmetry", *J. Fluid Mech.*, **409**, 1–12. https://doi.org/10.1017/S0022112099007831

Iollo, A., Ferlauto, M. and Zannetti, L. (2001), "An aerodynamic optimization method based on the inverse problem adjoint equations", *J. Comput. Phys.*, **173**, 87–115. https://doi.org/10.1006/jcph.2001.6845

Kothari, A., Tarpley, C. and McLaughlin, T. (1996), "Hypersonic vehicle design using inward turning flow fields", *AIAA Paper 1996-2552, 32nd Joint Propul. Conf., Buena Vista, FL.* https://doi.org/10.2514/6.1996-2552

Kuranov, A. and Korabelnikov, A. (2008), "Atmospheric cruise flight challenges for hypersonic vehicles under the AJAX concept", *J. Propul. Pow.*, **24**(6), 1229–1247. https://doi.org/10.2514/1.24684

Liu, J., Ding, F., Huang, W. and Jin, L. (2014), "Novel approach for designing a hypersonic gliding-cruising dual waverider vehicle", *Acta Astronaut.*, **102**, 81–88. https://doi.org/10.1016/j.actaastro.2014.04.024

Mölder, S. and Szpiro, E. (1966), "Busemann inlet for hypersonic speeds", *J.Spacecraft Rockets*, **3**(8), 1303–1304. https://doi.org/10.2514/3.28649

Poinsot, T. and Lele, S. (1992), "Boundary conditions for direct simulations of compressible viscous reacting flows", *J. Comput. Phys.*, **101**, 104–129. https://doi.org/10.1016/0021-9991(92)90046-2

Ramasubramanian, V., Starkey, R. and Lewis, M. (2008), "An Euler numerical study of Busemann and quasi-Busemann hypersonic inlets at on- and off-design speeds", *AIAA Paper 2008-66, 46th AIAA Aerosp. Sci. Meeting & Exhibit, Reno, NV.* https://doi.org/10.2514/6.2008-66

Smart, M. (1999), "Design of three-dimensional hypersonic inlets with rectangular-to-elliptical shape transition", *J. Propul. Pow.*, **15**(3), 408–416. https://doi.org/10.2514/2.5459

Smart, M.K. (2001), "Experimental testing of a hypersonic inlet with rectangular-to-elliptical shape transition", *J. Propul. Pow.*, **17**(2), 276–283. https://doi.org/10.2514/2.5774

Wang, C., Tian, X. and Yan, L. (2015), "Preliminary integrated design of hypersonic vehicle configurations including inward-turning inlets", *J. Aerospace Eng.*, **28**, 04014143. https://doi.org/10.1061/(ASCE)AS.1943-5525.0000480

Wang, J., Cai, J., Duan, T. and Tian, Y. (2017), "Design of shape morphing hypersonic inward-turning inlet using multistage optimization", *Aerospace Sci. Technol.*, **66**, 44–58. https://doi.org/10.1016/j.ast.2017.02.018

Xiong, B., Fan, X. and Wang, Y. (2019a), "Parameterization and optimization design of a hypersonic inward turning inlet", *Acta Astronaut.*, **164**, 130–141. https://doi.org/10.1016/j.actaastro.2019.07.004

Xiong, B., Ferlauto, M. and Fan, X. (2019b), "Parametric generation and computational analysis of

a REST inlet", *5th ECCOMAS Young Investig. Conf. (YIC2019), Krakow, Poland.*

You, Y. (2011), "An overview of the advantages and concerns of hypersonic inward turning inlets", *AIAA Paper 2011-2269 17th AIAA Int. Space Planes and Hypersonic Syst. and Techol. Conf., San Francisco, USA*. https://doi.org/10.2514/6.2011-2269

CC